Scaling of the translational velocity of vortex rings behind conical objects

Guillaume de Guyon and Karen Mulleners [*]

*École polytechnique fédérale de Lausanne, Institute of Mechanical Engineering,
Unsteady Flow Diagnostics Laboratory, 1015 Lausanne, Switzerland*

Ring vortices are efficient at transporting fluid across long distances. They can be found in nature in various ways: they propel squids, inject blood in the heart, and entertain dolphins. These vortices are generally produced by ejecting a volume of fluid through a circular orifice. The impulse given to the vortex rings moving away results in a propulsive force on the vortex generator. Propulsive vortex rings have been widely studied and characterized. After four convective times, the vortex moves faster than the shear layer it originates from and separates from it. When the vortex separates, the circulation of the vortex reaches a maximum value, and the nondimensional energy attains a minimum. The simultaneity of these three events obfuscates the causality between them. To analyze the temporal evolution of the nondimensional energy of ring vortices independent of their separation, we analyze the spatiotemporal development of vortices generated in the wake of cones. Cones with different apertures and diameters were accelerated from rest to produce a wide variety of vortex rings. The energy, circulation, and velocity of these vortices were extracted based on time-resolved velocity field measurements. The vortex rings that form behind the cones have a self-induced velocity that causes them to follow the cone, and they continue to grow as the cone travels well beyond the limiting vortex formation timescales observed for propulsive vortices. The nondimensional circulation, based on the vortex diameter, and the nondimensional energy of the drag vortex rings converge after three convective times to values comparable to their propulsive counterparts. This result proves that vortex pinch-off does not cause the nondimensional energy to reach a minimum value. The limiting values of the nondimensional circulation and energy are mostly independent of the cone geometry and translational velocity and fall within an interval of 10% around the mean value. The velocity of the vortex shows only 6% of variation and is the most unifying quantity that governs the formation of vortex rings behind cones.

I. INTRODUCTION

Vortex rings are ubiquitous phenomena widely observed in nature. Many sea creatures produce vortex rings to propel themselves efficiently. Squids, scallops, and salps eject water through a circular orifice, producing a high-velocity vortex ring and thus thrust [1,2]. Some fish release vortex rings in their wake by oscillating their tail and pectoral fins [3]. Vortex rings are also efficient at transporting fluid. The blood injected in the left ventricle of the heart forms a vortex ring, and any imperfection in the formation process is symptomatic of severe heart disease [4]. Extinguishing powder can be transported on distances superior to 100 m to extinguish oil well fires, by shooting a vortex ring along the axis of the burning gusher [5].

---

[*]karen.mulleners@epfl.ch

Vortex rings introduced above may be classified as propulsive vortices. They are generated by ejecting fluid through a circular orifice, or around a fin, and move away from the body they originate from. The momentum given to the fluid results in a propulsive force acting on the body. A second family of vortex rings emerges from this classification. Vortices are passively generated in the wake of a moving axisymmetric body. We refer to them as drag vortices. They are involved in slowing down the fall of dandelions, improving the seeding on long distances [6]. Vortex rings also form in the wake of parachutes when they deploy and can lead to the collapse of the parachute if not properly considered [7]. Vortex rings have been studied numerically and experimentally. The classical apparatus to study propulsive vortices is to push a volume of fluid out of a cylinder with a piston. A shear layer forms at the exit of the cylinder, then rolls up to create the vortex ring. Time is measured in a nondimensional form T^* as the ratio between the length of fluid pushed by the piston and the diameter of the exit. The vortex reaches a maximum circulation Γ at $T^* \approx 4$, also known as the vortex formation time. This timing is consistently reported for circulation-based Reynolds numbers Γ/ν superior to 2000, and for various piston acceleration profiles [8]. When the circulation reaches a maximum, the vortex no longer accepts vorticity from the shear layer, and this process is referred to as vortex separation.

A first explanation to the separation is derived from the Kelvin-Benjamin variational principle: a steadily translating vortex ring is the maximum state of kinetic energy E on a isovortical sheet with constant impulse I [9]. This approach led to the computation of the energy of the vortex with respect to its impulse and circulation, $E^* = E/\sqrt{I\Gamma^3}$. The vortex separates when the nondimensional energy E^* delivered by the piston falls below the energy of a steadily translating vortex ring [8]. The limiting nondimensional energy is consistently found at $0.3 \pm 15\%$ for circulation-based Reynolds numbers above 2000 [10]. The nondimensional energy quantifies the vorticity distribution inside the vortex. The lower the value of E^*, the more uniform the vorticity distribution is. For a Hill's spherical vortex, E^* has a low value of 0.16. When the shear layer starts to roll up, for $T^* < 1$, vorticity is concentrated near the vortex core and E^* has values above one. As the piston moves, more vorticity accumulates in the vortex and spreads towards the cylindrical symmetry axis, decreasing the value of E^*. There is a practical limit to the spreading of the vorticity, represented by this limit of $E^* = 0.3$. A possible interpretation of the vortex separation emerges from the study of the stability of vortex rings. Dynamical system analysis [11] and perturbation response of vortices from the Norbury family [12] showed that vorticity close to the axis of symmetry gets shed in the tail of the vortex, where the shear layer connects to the vortex. This could prevent the accumulation of additional vorticity by the vortex.

The second explanation for the vortex separation is based on a kinematic argument. The vortex separates when it is traveling faster than the shear layer. The velocity of the shear layer is usually estimated to half of the piston velocity [13]. For $E^* \approx 0.3$ the critical separation velocity was calculated at 59% of the piston velocity [14]. The translational velocity of the vortex ring depends on its nondimensional energy. Saffman [15] estimated the velocity U_0 of a viscous steady vortex ring by the relation

$$E = 2U_0 I - \frac{3}{8}D_0\Gamma^2 \tag{1}$$

with D_0 being the diameter of the vortex ring. This equation is equivalent to

$$U_0 = \frac{\Gamma}{\pi D_0}\left(E^*\sqrt{\pi} + \frac{3}{4}\right). \tag{2}$$

Both energetic and kinematic explanations to the vortex separation are connected, and it is not obvious to assess the causality between vorticity spreading, vortex velocity, and vortex separation.

The tools developed to study propulsive vortices have not been as extensively applied to the analysis of drag vortices. An apparent reason is that drag vortices do not separate in the same timescale. Drag vortex rings are usually studied by accelerating a flat plate or a disk in a fluid [16,17]. During the first convective times, the vortex created in the wake of the disk develops in a
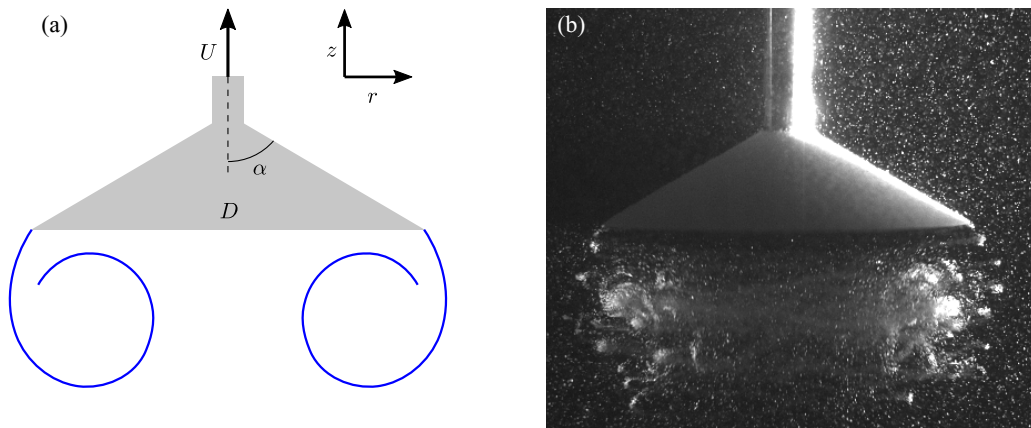
FIG. 1. (a) Sketch of the cone and the ring vortex generated in its wake indicating the relevant experimental parameters: cone diameter D, cone aperture α, and constant final cone translation velocity U. The direction of U indicates the upward motion of the cone in the quiescent volume of water. (b) Raw image of the seeding particles accumulating in the main vortex ring and highlighting the small-scale shear layer vortices. This raw image was taken after seeding particles had settled on the cone and was not used for processing.

similar way as propulsive vortices. Around $T^* = 4$ the circulation starts increasing at a lower rate, but does not converge, and is not followed by vortex separation [18]. For diameter-based Reynolds numbers ranging from 1600 to 4000, the nondimensional energy decreases down to values between 0.28 and 0.35 [19]. Later, past $T^* = 10$, azimuthal instabilities break the axisymmetry and lead to separation of the vortex.

We propose to experimentally extend the analysis performed on propulsive vortices to drag vortices. Cones of different apertures, diameters, and velocities will be translated to produce a wide variety of vortex rings in their wake. The nondimensional energy will be measured to assess if it converges to a lower limit when the vortex stays close to its feeding shear layer. This information will help us to understand the causality between vortex separation, vortex velocity, and vorticity distribution in a propulsive vortex ring. A scaling of the vortex circulation, energy, and velocity will be performed to identify the most relevant parameters among the geometry and the kinematics of both the cone and the vortex.

II. EXPERIMENT

A cone is immersed in water and translated along its axis of symmetry [Fig. 1(a)]. The translation is performed by a belt-driven linear actuator, powered by a NEMA 17 stepper motor. The cones are 3D printed, their diameters D range from 3 cm to 9 cm, and their aperture α from $30°$ to $90°$. They are accelerated at $3 \, \mathrm{m \, s^{-2}}$ from rest, up to velocities U ranging from $0.35 \, \mathrm{m \, s^{-1}}$ to $0.70 \, \mathrm{m \, s^{-1}}$. The duration of the acceleration phase varies from 0.12 s to 0.22 s between the fastest and the slowest moving cones. A series of 18 experiments were conducted, with diameter-based Reynolds numbers $\mathrm{Re}_D = UD/\nu$ comprising between 1×10^4 and 6×10^4.

Particle image velocimetry (PIV) is carried out in a symmetry plane in the wake of the cone during its translation. The water is seeded with $30 \, \mu\mathrm{m}$ aluminium oxide particles which are illuminated with two light-emitting diodes (LEDs). Figure 1(b) shows a raw image from one of the cameras, which clearly pictures concentrations of seeding particles indicating small-scale shear layer vortices that accumulate into a large-scale coherent ring vortex. The high concentration of particles in this image is the result of the deposit of the particles on the cone during a break in the measurements. This image serves as a beautiful visualization of the main vortex ring and the small-scale shear

layer vortices that feed into it but is not suitable for PIV analysis. Only measurement series with homogenous seeding particle distributions have been considered for further analysis.

A field of view of $18 \, \mathrm{cm} \times 36 \, \mathrm{cm}$ is recorded at $1000 \, \mathrm{fps}$ by two high-speed cameras, each recording one half of the cone trajectory with a definition of $1024 \, \mathrm{px} \times 1024 \, \mathrm{px}$. The cameras are positioned such that the fields of view touch but do not overlap. The images are processed with a multigrid algorithm and a final interrogation window size of $24 \, \mathrm{px} \times 24 \, \mathrm{px}$ with an overlap of 60%, producing a grid of 100×200 velocity vectors with a physical resolution of 1.8 mm between adjacent vectors. This vector spacing corresponds to 6% of the smallest cone diameter.

The length L traveled by the cone is recorded and used here to define the nondimensional timing of the experiment: $T^* = L/D$. The cones reach their maximum velocity U after $T^* = 0.22$ for large slow cones and after $T^* = 2.34$ for small fast cones. For reference, the nondimensional time at which the vortex properties converge is around $T^* \approx 3$. Particle image velocimetry gives access to the velocity field (u, v), from which the vorticity field ω is derived. The stream function ψ, later used to compute the energy of the vortex, is obtained by integrating the Cauchy-Riemann relations in cylindrical coordinates:

$$u = \frac{1}{r} \frac{\partial \psi}{\partial r}, \quad v = -\frac{1}{r} \frac{\partial \psi}{\partial z}. \tag{3}$$

III. RESULTS

A. Spatial and temporal development of a drag vortex ring

The results presented in this section focus first on the detailed analysis of a single experiment, for a cone of aperture $\alpha = 45°$, diameter $D = 6 \, \mathrm{cm}$, and velocity $U = 0.5 \, \mathrm{m\,s^{-1}}$. The corresponding Reynolds number $\mathrm{Re}_D = 3 \times 10^4$ is in the middle range of the study. Results from all the experiments are compared in the next section.

When the cone is pulled up, fluid moves around it and high-velocity gradients rise at the tip of the cone. A shear layer forms and rolls up behind the cone, creating a vortex ring in the wake. With a diameter-based Reynolds number superior to 1×10^4, the shear layer breaks into small-scale vortices ($\sim$1 mm) due to a Kelvin-Helmholtz instability. The smaller vortices are directly visible on the raw image from the camera [Fig. 1(b)], but are smaller than the output PIV resolution of 1.8 mm. These instabilities have no effect on the accumulation of vorticity in the vortex [10,20].

The vortex contour is determined using Lagrangian methods. A finite-time Lyapunov exponent (FTLE) analysis has been applied to accurately delimit vortices produced by various vortex generators [21–24]. The vortex is delimited by the positive FTLE ridge and the base of the cone (Fig. 2). This contour contains not only vortical fluid but also entrained fluid with low or zero vorticity. Nonvortical fluid is pulled along in the wake of the cone during the initial acceleration from rest. This nonvortical fluid initially sits below the cone, delimited by the virtual line in Fig. 2(a). The integration of this line trajectory delimits the volume of nonvortical fluid from the volume of vortical fluid injected in the vortex at the tip of the cone. The nonvortical volume of fluid, indicated by light gray area in Figs. 2(b)–2(f), is entrained and progressively mixed with the vortical fluid. At $T^* = 0.5$ [Fig. 2(b)], the nonvortical fluid accounts for 38% of the volume of the vortex. At $T^* = 3$ [Fig. 2(g)] there is no more nonvortical fluid. Vorticity has then fully spread throughout the vortex.

The consequences of the spreading of the vorticity are analyzed by calculating the vortex circulation $\Gamma = \iint \omega \, dr \, dz$. The surface integration is performed on each side of the $r = 0$ axis, on the domain delimited by the FTLE contour and the cone base. The absolute values obtained on both sides of the symmetry axis are averaged to obtain a final circulation value. The nondimensional circulation Γ/UD increases up to values around 2.3 [Fig. 3(e)]. The growth rate of the circulation $\dot{\Gamma}$ decreases progressively. Around $T^* = 1$, a maximum growth rate $\dot{\Gamma} = 1.2U^2$ is reached. After $T^* = 3$ the rate stabilizes around $\dot{\Gamma} = 0.06U^2$. The stabilization starts when the nonvortical volume of fluid V_0 inside the vortex volume V vanishes.
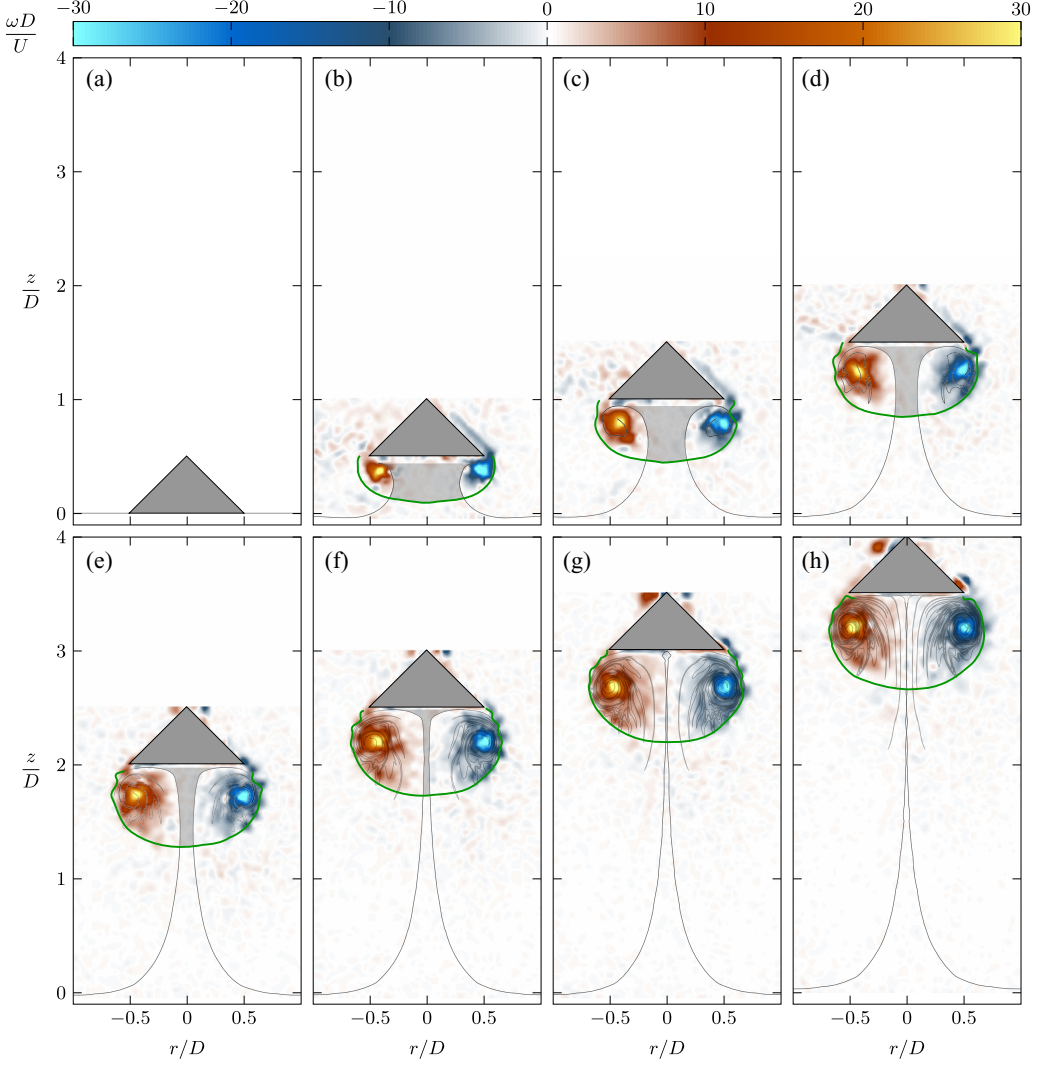
FIG. 2. Growth of a vortex ring in the wake of a translating cone of $D = 6\,\text{cm}$, $\alpha = 45°$, $\text{Re}_D = 3 \times 10^4$. The green line delimits the contour of the vortex based on FTLE. The light gray area from (b) to (f) highlights the nonvortical volume of fluid in the vortex and outlines the spreading of vorticity over time.

Similar observations where made on vortex rings generated by piston cylinders: at $T^* = 4$, the circulation reaches a maximum $\Gamma/UD \approx 2.3$ and the vorticity spreads up to the cylindrical symmetry axis. The vortex separation for propulsive vortices is attributed to the tail shedding resulting from the vorticity spread [8]. In the present experiment, no separation occurs because the vortex translational velocity is directed towards the cone. The vortex stays in the vicinity of the shear layer and keeps growing and accumulating vorticity after $T^* = 3$ [Figs. 3(c) and 3(d)].

The extension of the vortex is quantified by observing the vortex center (Z_0, R_0), calculated as

$$Z_0 = \frac{\iint \omega z r^2 \, dr \, dz}{\iint \omega r^2 \, dr \, dz}, \qquad R_0^2 = \frac{\iint \omega r^2 \, dr \, dz}{\iint \omega \, dr \, dz}, \qquad D_0 = 2R_0. \qquad (4)$$
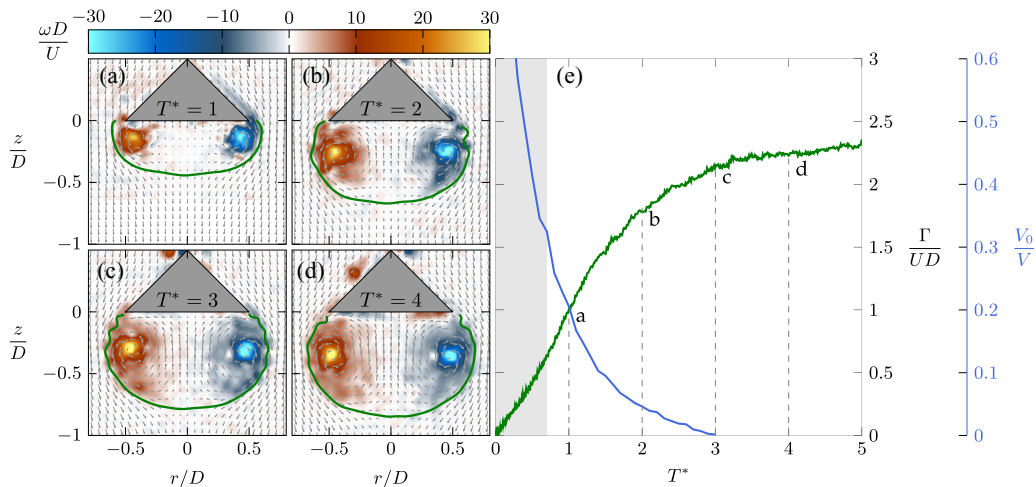
FIG. 3. Vorticity field and vortex boundary in the wake of a translating cone with $\alpha = 45°$, $D = 6\,\text{cm}$, and $U = 0.5\,\text{m s}^{-1}$ at (a) $T^* = 1$, (b) $T^* = 2$, (c) $T^* = 3$, and (d) $T^* = 4$. (e) Temporal evolution of the nondimensional vortex circulation Γ/UD and the volume of nonvortical fluid V_0 relative to the total vortex volume V. The gray area indicates the acceleration phase of the cone.

The integrations are performed on each half of the $r = 0$ axis, on the domain delimited by the FTLE contour and the cone base. The absolute values obtained on both sides of the symmetry axis are averaged to obtain the final values. Positions are given relative to the base of the cone [Fig. 4(b)].

The vortex center [Fig. 4(a)] quickly moves away from the cone and has traveled a distance of $0.22D$ at $T^* = 1$. It progressively slows down, and for $T^* > 3$, the vortex center moves away from the cone and the axis of symmetry at a more constant velocity. A distance of $0.03D$ is covered between $T^* = 4$ and $T^* = 5$. The increase of the vortex diameter suggests that the cone diameter is not the most suitable parameter for nondimensionalization of the circulation. Using the vortex diameter D_0, the nondimensional circulation reaches a maximum value of 2.2 at $T^* = 3$ and stays constant, whereas the nondimensional circulation based on D continues to grow [Fig. 4(b)]. The term Γ/D_0 has the dimension of a velocity and is featured in Eq. (2). It quantifies the influence of the vortex circulation and dimension on the velocity of the ring.

The other parameter that influences the velocity of the vortex ring is the nondimensional energy of the vortex E^*. It represents the energy E relative to impulse I and circulation Γ:

$$ I = \pi \iint \omega r^2 \, dr \, dz, \quad E = \pi \iint \psi \omega \, dr \, dz, \quad E^* = \frac{E}{\sqrt{I\Gamma^3}}. \tag{5} $$

The nondimensional energy quantifies the distribution of the vorticity inside the vortex. It is compared to a more statistical definition of the vorticity distribution: the standard deviation of the vorticity σ_ω relative to its average $\bar{\omega}$. The evolution of E^* and $\sigma_\omega/\bar{\omega}$ are presented in Fig. 5(a). The nondimensional energy and relative vorticity distribution have a similar evolution, and an empirical relation $\sigma_\omega/\bar{\omega} = 2.3E^* + 0.5$ can be derived. Although this relation is specific to this experiment, it confirms that E^* is a valid quantifier of vorticity distribution. During the first convective time, the shear layer starts to roll up and vorticity is concentrated in the vortex core. Nondimensional energy has high values around 0.7. As vorticity keeps accumulating in the vortex, E^* continuously drops towards a limiting value of 0.3, reached at $T^* = 3$. A minimal value between 0.27 and 0.35 was also observed for vortex rings generated by piston cylinders [8,25,26] and corresponds to the moment when the vortex separates from its feeding shear layer. This limit on E^* answers one of the questions that motivated this experiment: the nondimensional energy of a vortex ring does not decrease further, even if it stays connected to its feeding shear layer. Contrary to vortex rings generated by piston
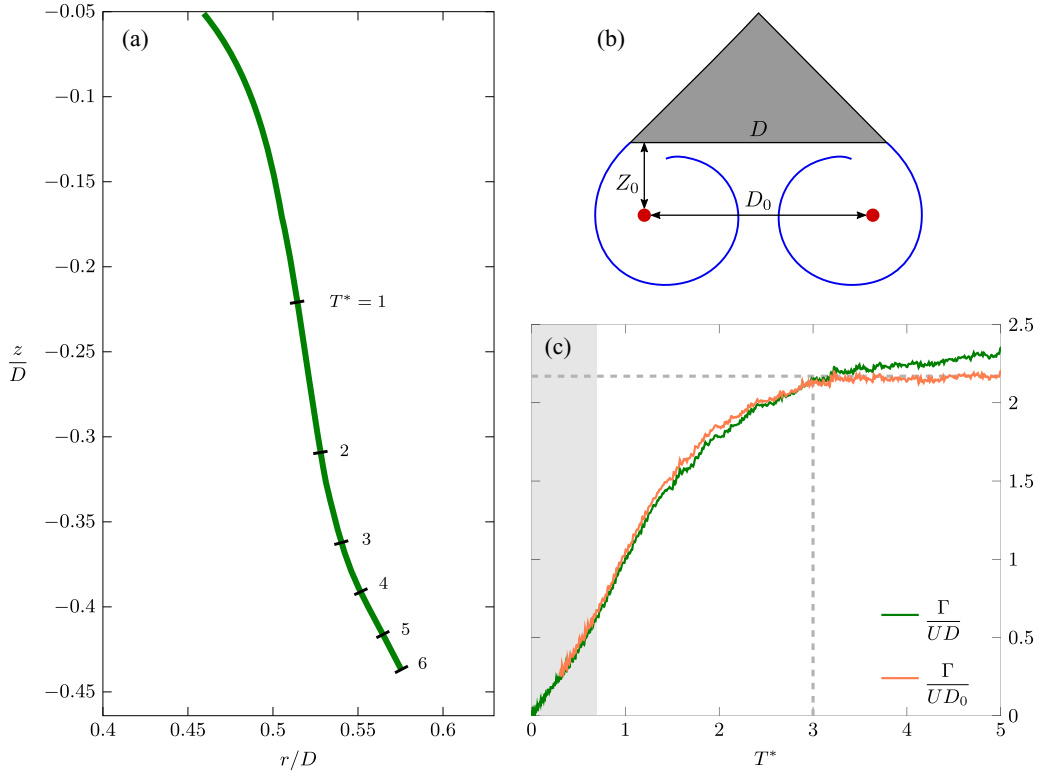
FIG. 4. (a) Trajectory of the vortex center relative to the cone for $\alpha = 45°$, $D = 6$ cm, and $U = 0.5$ m s^{-1}. (b) Parametrization of the vortex center. (c) Circulation of the vortex, nondimensionalized using the cone diameter D and the vortex diameter D_0. The gray area indicates the acceleration phase of the cone.
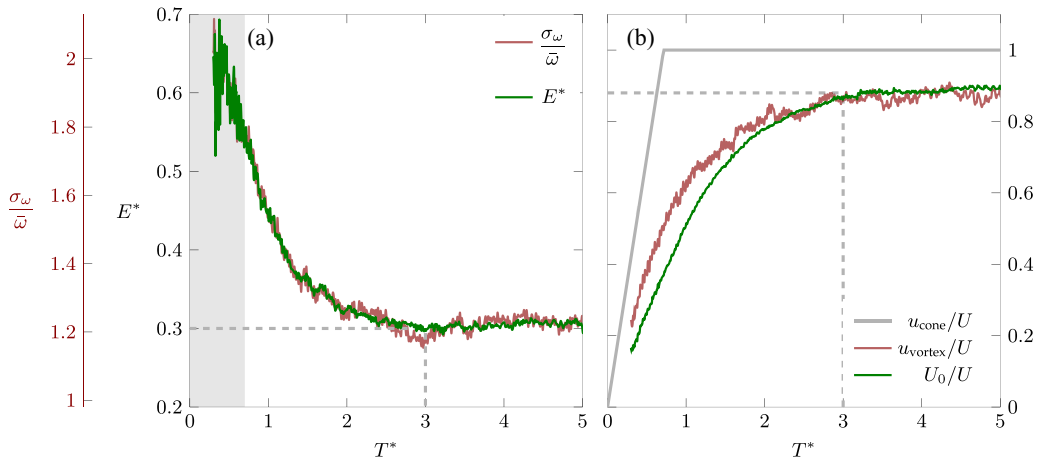

FIG. 5. (a) Temporal evolution of the nondimensional energy and relative vorticity distribution. The gray area indicates the acceleration phase of the cone. (b) Theoretical and measured velocity of the vortex, relative to the maximum cone velocity. The evolution of the translation velocity of the cone is added for reference.

cylinders, vorticity still accumulates in the vortex at a low rate, without a noticeable effect on the vorticity distribution.

The quantities Γ/D_0 and E^* characterize, respectively, the overall vorticity present in the vortex and the distribution of the vorticity in the vortex. Both reach a limiting value at $T^* = 3$. As a consequence, the theoretical translational velocity U_0 of the vortex ring, derived from Saffman [15], also reaches a steady value:

$$U_0 = \frac{\Gamma}{\pi D_0}\left(E^*\sqrt{\pi} + \frac{3}{4}\right). \tag{6}$$

The theoretical velocity Eq. (6) is compared with the measured vortex velocity u_{vortex}, obtained by averaging the axial velocity component inside the vortex volume. Both theoretical and measured velocities converge to a value of $0.9U$ [Fig. 5]. The theoretical velocity underestimates the measured velocity during the transient phase, due to the fact that Eq. (6) is valid only for a steady vortex ring.

Since the vortex stays attached to the cone, the velocity deficit of the vortex compared to the cone should not be interpreted as a vortex separation, but rather as an increase of the vortex volume.

B. Scaling of the vortex characteristics

The influence of the cone geometry and kinematics on the vortex circulation, nondimensional energy, and velocity are analyzed in this section. A discussion of the influence of the vortex detection method on the integral values and an estimation of the experimental uncertainty is presented in the Appendix A. All experiments are sorted by their circulation-based Reynolds number. As seen in the previous section, the circulation does not reach a clear maximum, but Γ/D_0 does. We therefore introduce a Reynolds number $\text{Re}_\Gamma = \frac{\Gamma D}{\nu D_0}$ based on the maximum value of Γ/D_0.

Different cone apertures were used, from $\alpha = 30°$ to $\alpha = 90°$ (flat disk). The trajectory of the vortex center is extracted for four cones of different aperture and identical diameter $D = 6$ cm and velocity $U = 0.5$ m s^{-1} [Fig. 6]. The four trajectories show an increase of the vortex diameter past $T^* = 2$. A larger cone aperture leads to a larger vortex diameter because the cone deviates the flow more in the radial direction. At $T^* = 3$ the vortex radius ranges from $D_0 = 0.88D$ at $\alpha = 30°$ to $D_0 = 1.1D$ at $\alpha = 90°$.

The maximum nondimensional circulation Γ/UD_0 is calculated for all cases and presented in Fig. 6(b). All values presented in Figs. 6(b)–6(d) are obtained after the cone has reached its final constant velocity. The average value is 2.26, with variations of $\pm 9\%$. Cones with an aperture of $90°$, or disks, exhibit lower nondimensional circulations. For structural reasons they are not strictly disks: they have a thickness of $0.06D$ and a reverse sweep of $30°$. This sweep is believed to be responsible for the lower nondimensional circulation of the disk compared to the cones. The effect is reversed for the nondimensional energy. Disks have slightly higher values [Fig. 6(c)]. The Nondimensional energy converges on average to a minimum of 0.3, with variations of $\pm 12\%$.

The nondimensional circulation and energy are largely independent on the Reynolds number. Similar behavior is observed for vortices generated by piston cylinders. For various simulations with $\text{Re}_\Gamma > 2000$, nondimensional circulation and energy were recorded to have variations of, respectively, $\pm 10\%$ and $\pm 15\%$ [10].

From the circulation and the nondimensional energy, the theoretical velocity U_0 of the vortex ring is computed [Eq. (6)]. The relative velocity U_0/U has an average of 0.93, within an interval of $\pm 6\%$ [Fig. 6(d)]. The interval of variation is smaller than the ones of Γ/UD_0 ($\pm 9\%$) and E^* ($\pm 12\%$). The variations in nondimensional circulation and nondimensional energy compensate to produce a regular relative velocity. In particular the disks, which have higher nondimensional energy and lower circulation, have a relative velocity equivalent to the cones. This suggests that the cone's velocity is a better scaling parameter than the nondimensional circulation or energy.
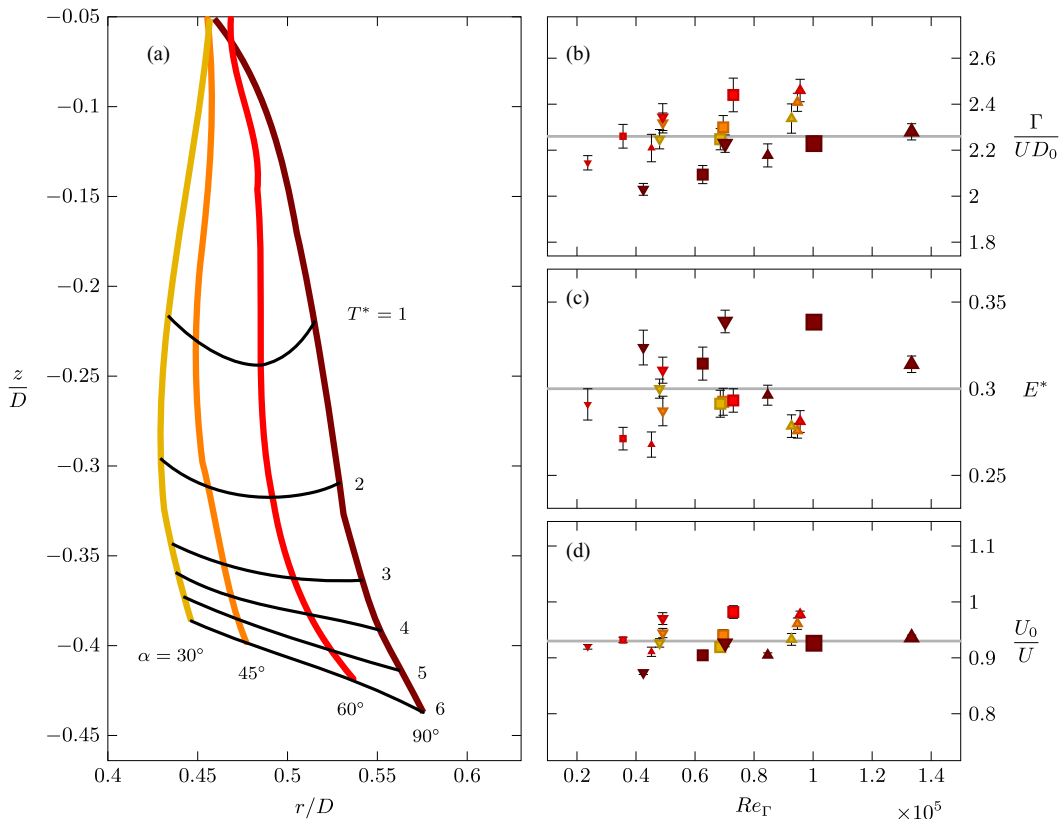
FIG. 6. (a) Vortex center trajectories for four aperture angles, at $D = 6\,\text{cm}$ and $U = 0.5\,\text{m s}^{-1}$. (b–d) Maximum circulation, minimum nondimensional energy, and maximum theoretical vortex velocity for all experiments. The gray lines indicate the average value across all parameter variation. The error bars reflect the uncertainty on the converged values quantified as explained in Appendix B. The shape of the markers indicates the final translation velocity of the cone: $\triangledown$: $U = 0.35\,\text{m s}^{-1}$, $\square$: $U = 0.5\,\text{m s}^{-1}$, $\triangle$: $U = 0.65\,\text{m s}^{-1}$. The size of the markers reflects the diameter of the cone: $\circ$: $D = 3\,\text{cm}$, $\bigcirc$: $D = 6\,\text{cm}$, $\bigcirc$ $9\,\text{cm}$.

IV. CONCLUSION

A vortex ring produced by a piston cylinder simultaneously separates, reaches a minimal nondimensional energy, and outpaces its feeding shear layer. The simultaneity of these three events obfuscates the causality between them. To analyze the temporal evolution of the nondimensional energy of ring vortices independent of their pinch-off, we focused on vortices generated in the wake of cones. Cones with different apertures and diameters were accelerated from rest to produce a wide variety of vortex rings. The initial development and growth of these vortex rings were studied experimentally using time-resolved velocity field measurements.

The vortex rings that form behind the cones have a self-induced velocity that cause them to follow the cone beyond the typical vortex formation timescales observed for vortex rings emanating from a piston cylinder apparatus. Another difference is that propulsive vortex rings reach a maximum in circulation but the circulation of drag vortex rings keeps increasing and does not reach a clear plateau. However, for $T^* > 3$, the circulation of drag vortices increases proportionally to the vortex size, and the circulation nondimensionalized by the vortex diameter Γ/UD_0 converges to a limiting value between 2.05 and 2.45. The nondimensional energy is linearly related to the relative standard deviation of the vorticity, demonstrating that E^* is a measure of vorticity distribution inside the
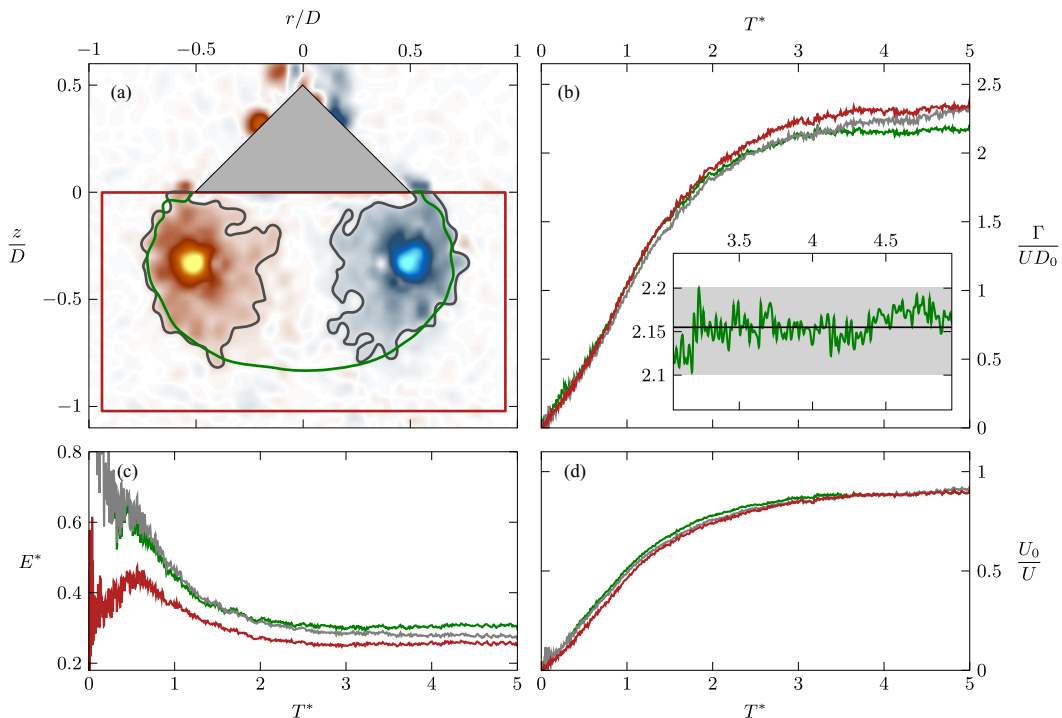
FIG. 7. (a) Vorticity field at $T^* = 3$ and contours used to compute vortex characteristics including the FTLE ridge (—), isocontour of vorticity $|\omega D/U| = 1$ (—), and a rectangular box (—). (b) Temporal evolution of the nondimensional circulation, (c) nondimensional energy, and (d) theoretical vortex velocity relative to the cone velocity. The inset in (b) zooms in on the convergence for the circulation calculated within the FTLE boundary. The black line indicates the average value between $T^* = 3$ and $T^* = 5$ and is considered as the converged circulation result. The amplitude of the variations are outlined by the gray rectangle, and this is considered as the uncertainty for the measured circulation values.

vortex ring. At the start of the vortex formation, vorticity is concentrated near the vortex core and E^* is at its highest. In time, the vortex grows and the vorticity distribution spreads, which is reflected by a decrease in E^*. The nondimensional energy converges around $T^* = 3$ to a minimum value between 0.27 and 0.35. Similar values of nondimensional circulation and energy were observed for vortices produced by piston cylinders. This results proves that vortex pinch-off does not cause the nondimensional energy to converge to a minimum value.

The nondimensionalized energy, circulation, and velocity of the ring vortices reach constant values independent of the cone diameter, aperture angle, and translational velocity when scaled based on the vortex diameter instead of the cone diameter. The limiting values of the circulation and the energy experience variations of 9% and 12% across the tested parameter range. These variations compensate each other to produce a constant vortex velocity of $U_0 = 0.93U \pm 6\%$. The difference between the vortex velocity and the cone velocity does not indicate vortex separation but is the result of the spatial growth of the vortex. The vortex velocity is the most unifying quantity to scale and predict the development of vortex rings behind various cone geometries.

APPENDIX A: SENSITIVITY TO THE VORTEX DETECTION METHOD

To estimate the uncertainty of the scaling values computed in this article [Eqs. (4) and (5)] and their sensitivity to the selection of the integration contour, we compare here the results for three

different integration contours. The contour that is used for the final results presented in Fig. 6 is the FTLE contour. In addition to the FTLE contour, we consider here the iso-vorticity contour $|\omega D/U| = 1$ and a rectangular contour of dimensions $1.8D \times D$ [Fig. 7(a)]. The iso-vorticity contour is slightly wider than the FTLE one and contains also vorticity patches outside of the FTLE contour that will be convected into the wake. The rectangular box is the easiest contour to use, but it will also contain vorticity that should not be considered as part of the vortex. The rectangular and vorticity contours both contain more vorticity that the FTLE contour encloses, resulting in higher circulations and larger vortex diameters. At $T^* = 4$, the nondimensional circulation is, respectively, 7% and 4% higher than with the FTLE method [Fig. 7(b)]. The effect is reversed for the nondimensional energy, as the vorticity added by the larger contours is of low value and more uniform than in the vortex core [Fig. 7(d)]. For the rectangular and the iso-vorticity contour, E^* is, respectively, 16% and 9% lower. Variations in circulation and nondimensional energy compensate in the computation of the velocity [Fig. 7(c)]. Both the rectangular and the iso-vorticity contour result in the same converged velocity value within 3% of the one computed on the FTLE contour. The standard deviation of the bias introduced by the choice of the integration contour is 1.5% for the tested parameter space and can be considered constant and does not affect the conclusion of the paper.

APPENDIX B: ACCURACY OF THE CONVERGENCE

The nondimensional circulation, energy, and vortex velocity presented in Figs. 6(b)–6(d) are all extracted from their converged values. The converged value is obtained by averaging the quantity between $T^* = 3$ and $T^* = 5$ [Fig. 7(b)]. The full range of variations measured between $T^* = 3$ and $T^* = 5$ determines the uncertainty on the convergence value and is represented by the error bars in Figs. 6(b)–6(d). The maximum uncertainty is 3% for the nondimensional circulation, 4% for the nondimensional energy, and 1% for the relative velocity of the vortex.

---

[1] B. Y. W. Johnson, P. D. Soden, and E. R. Trueman, A study in jet propulsion: An analysis of the motion of the squid, *Loligo vulgaris*, J. Exp. Biol. **56**, 155 (1972).

[2] P. F. Linden and J. S. Turner, 'Optimal' vortex rings and aquatic propulsion mechanisms, Proc. R. Soc. B **271**, 647 (2004).

[3] G. V. Lauder and E. G. Drucker, Forces, fishes, and fluids: Hydrodynamic mechanisms of aquatic locomotion, News Physiol. Sci. **17**, 235 (2002).

[4] J. O. Dabiri, Optimal vortex formation as a unifying principle in biological propulsion, Annu. Rev. Fluid Mech. **41**, 17 (2009).

[5] D. G. Akhmetov, B. A. Lugovtsov, and V. F. Tarasov, Extinguishing gas and oil well fires by means of vortex rings, Combust. Explos. Shock Waves **16**, 490 (1980).

[6] C. Cummins, M. Seale, A. Macente, D. Certini, E. Mastropaolo, I. M. Viola, and N. Nakayama, A separated vortex ring underlies the flight of the dandelion, Nature (London) **562**, 414 (2018).

[7] H. Higuchi, H. Balligand, and J. H. Strickland, Numerical and experimental investigations of the flow over a disk undergoing unsteady motion, J. Fluid. Struct. **10**, 705 (1996).

[8] M. Gharib, E. Rambod, and K. Shariff, A universal time scale for vortex ring formation, J. Fluid Mech. **360**, 121 (1998).

[9] T. B. Benjamin, The alliance of practical and analytical insights into the nonlinear problems of fluid mechanics, in *Applications of Methods of Functional Analysis to Problems in Mechanics*, edited by P. Germain and B. Nayroles (Springer, Berlin, Heidelberg, 1976), pp. 8–29.

[10] K. Mohseni, H. Ran, and T. Colonius, Numerical experiments on vortex ring formation, J. Fluid Mech. **430**, 267 (2001).

[11] K. Shariff, A. Leonard, and J. H. Ferziger, Dynamical systems analysis of fluid transport in time-periodic vortex ring flows, Phys. Fluids **18**, 047104 (2006).

[12] C. O'Farrell and J. O. Dabiri, Perturbation response and pinch-off of vortex rings and dipoles, J. Fluid Mech. **704**, 280 (2012).

[13] K. Mohseni and M. Gharib, A model for universal time scale of vortex ring formation, Phys. Fluids **10**, 2436 (1998).

[14] M. Shusser and M. Gharib, Energy and velocity of a forming vortex ring, Phys. Fluids **12**, 618 (2000).

[15] P. G. Saffman, The velocity of viscous vortex rings, Stud. Appl. Math. **49**, 371 (1970).

[16] J. N. Fernando and D. E. Rival, Reynolds-number scaling of vortex pinch-off on low-aspect-ratio propulsors, J. Fluid Mech. **799**, R3 (2016).

[17] M. J. Ringuette, M. Milano, and M. Gharib, Role of the tip vortex in the force generation of low-aspect-ratio normal flat plates, J. Fluid Mech. **581**, 453 (2007).

[18] H. Johari and K. Stein, Near wake of an impulsively started disk, Phys. Fluids **14**, 3459 (2002).

[19] A. L. Yang, L. B. Jia, and X. Z. Yin, Formation process of the vortex ring generated by an impulsively started circular disc, J. Fluid Mech. **713**, 61 (2012).

[20] G. A. Rosi and D. E. Rival, Entrainment and topology of accelerating shear layers, J. Fluid Mech. **811**, 37 (2017).

[21] M. A. Green, C. W. Rowley, and A. J. Smits, The unsteady three-dimensional wake produced by a trapezoidal pitching panel, J. Fluid Mech. **685**, 117 (2011).

[22] S. Krishna, M. A. Green, and K. Mulleners, Flowfield and force evolution for a symmetric hovering flat-plate wing, AIAA J. **56**, 1360 (2018).

[23] C. O'Farrell and J. O. Dabiri, A Lagrangian approach to identifying vortex pinch-off, Chaos **20**, 017513 (2010).

[24] S. C. Shadden, J. O. Dabiri, and J. E. Marsden, Lagrangian analysis of fluid transport in empirical vortex ring flows, Phys. Fluids **18**, 047105 (2006).

[25] I. Danaila, F. Luddens, F. Kaplanski, A. Papoutsakis, and S. S. Sazhin, Formation number of confined vortex rings, Phys. Rev. Fluids **3**, 094701 (2018).

[26] M. Nitsche, Self-similar shedding of vortex rings, J. Fluid Mech. **435**, 397 (2001).